Supplement of Atmos. Chem. Phys., 18, 9929–9954, 2018
https://doi.org/10.5194/acp-18-9929-2018-supplement

Atmospheric Chemistry and Physics
Open Access
EGU

Supplement of

Gas-phase composition and secondary organic aerosol formation from standard and particle filter-retrofitted gasoline direct injection vehicles investigated in a batch and flow reactor

Simone M. Pieber et al.

Correspondence to: Simone M. Pieber (simone.pieber@psi.ch) and André S. H. Prévôt (andre.prevot@psi.ch)

S1. Emission Factors (EFs)

Emission factors from batch experiments were calculated based on a carbon mass balance as described in Platt et al. (2013) and Platt et al. (2017) (Eq. (S1)), where P is the species of interest, ωc the carbon fraction (0.85) of the fuel and CO_2 and CO, NMOC and eBC in units of carbon mass.

$$\mathrm{EF} = \frac{\Delta P}{\Delta CO2 + \Delta CO + \Delta NMOC + \Delta eBC} * \omega c \quad \text{(S1)}$$

Regulatory emission factors from the test bench were provided in accordance with the ECE Regulation No. 83, and use a fuel consumption of the vehicle in accordance with the ECE Regulation No. 101 and an effective fuel density of 0.75 kg L^{-1}.

S2. Test bench instrumentation (extended)

Gaseous components were monitored with an exhaust gas measuring system Horiba MEXA-9400H, including measurements of CO and CO_2 by infrared analyzers (IR), hydrocarbons by flame ionization detector (FID) for total hydrocarbon (THC) and non-methane hydrocarbon (NMHC) measurements, NO/NO_x with a chemoluminescence analyzer (CLA) which was not heated and applicable only for diluted gas, and O_2 (Magnos). The dilution ratio in the CVS-dilution tunnel was variable and controlled by means of the CO_2-analysis as described in the main text. Non-legislated gaseous emission components were analyzed by an FTIR (Fourier Transform Infrared Spectrometer, AVL SESAM) at the exhaust tailpipe, offering time-resolved measurement of approx. 30 emission components, including NO, NO_2, NO_x, NH_3, N_2O, HCN, HNCO, HCHO. Number concentration of non-volatile particles was measured with condensation particle counters (CPC) behind a thermo-conditioner heating the sample to 300°C (following the requirements of the PMP- Particle Measurement Program of the ECE GRPE Group).

S3. Sampling materials and length

- Tubing to sample direct emissions from the vehicle tailpipe for injection into the SC or online-OFR, or direct gas-phase measurements were made of SilcoTek®-coated steel (12 mm diameter), temperature controlled at 140°C and operated under high flows (30 L min^{-1}) to avoid substantial losses over the sampling length of roughly 8 m. Ejector dilutor 1 was placed in a temperature controlled housing (200°C), and ejector dilutor 1 operated at 80°C.
- Instruments sampling either from the SC, behind the OFR, or directly from the dilution system were connected via specific tubing for gas-phase and particle phase. Particle-phase tubing was made of stainless steel (6 mm diameter), and up to 2 m length. Support pumps were used at the instrument inlets, to minimize sampling residence time by increasing the flow rate. Total tubing length to reach all of the gas-phase instrument inlets, which were likewise equipped with

support pumps was up to 2 m. Tubing was made of Teflon or SilcoTek®-coated steel. The sampling line of the PTR-ToF-MS instrument and FID was temperature controlled at 60°C.

- SilcoTek®-coating and Teflon are suitable for sampling of species known to be easily retained on surfaces, such as formaldehyde, acetic acid, acetaldehyde, for which otherwise, in addition to the uncertainties of PTR-ToF-MS analysis, also tubing losses could induce a shift in our gas-composition analysis.
- The sampling system between the SC and OFR (for OFR-from-SC experiments) was made of a combination of SilcoTec® coated steel and conductive Teflon tubing, suitable for simultaneous gas- and particle phase sampling. The total length between SC and OFR inlet was roughly 35 cm (6 mm diameter, ca. 8 L min^{-1} flow). Additionally, all measurements from the dark SC batch sample were performed for at least 10 minutes, to reach a stable signal.

S4. OFR data quality (OH exposure, non-OH losses and NOx influence)

Several recent studies (Li et al., 2015; Peng et al., 2016; Peng et al., 2015) have estimated the contribution of alternative reaction processes than OH radical-induced ones in the OFR across a range of operating conditions (residence time, water vapor availability, and external OH reactivity (OHR_{ext}), which is the available OH-reactive material). These non-OH processes include reaction with photons (185 nm, 254 nm), and reactions with oxygen allotropes (excited oxygen atoms ($O(^1D)$), ground state oxygen atoms ($O(^3P)$), ozone (O_3)) were identified as relevant loss processes to precursor molecules. Under certain operating conditions, also suppression of OH formation is critical. We applied a previously published model (Li et al., 2015; Peng et al., 2016; Peng et al., 2015) to estimate competing reaction with OH and loss of precursor molecules by non-OH sources, and estimated the influence of NO_x based on Peng and Jimenez (2017). Details on model input parameters are presented in the following:

(a) OFR-from-SC (see results in Figure S11). As input to the model we used OHR_{ext}=100 s^{-1}, $[O_3]$=1.97x10^{14} molec cm^{-3} (corresponding to 8 ppm at 100% UV intensity), a water mixing ratio=0.01 (1% absolute humidity, corresponding to 50% RH at 25°C) and a residence time=100 sec. O_3 measured at our reactor output for 70% UV intensity was 0.74x10^{14} molec cm^{-3} (3 ppm), and at 50% UV intensity 0.17x10^{14} molec cm^{-3} (0.7 ppm). OHR_{ext} was calculated following Eq. (S2).

$$OHR_{ext} = \sum_i (c_{NMOC,i} * k_{OH,NMOC,i});$$

i=BENZ, TOL, XYL/EBENZ, C3-BENZ, CO, BuOH-D9 (S2)

where k_{OH} of benzene (BENZ), toluene (TOL), xylene/ethylbenzene (XYL/EBENZ), C3-benzene (C3-BENZ) are given in Table 2; here we applied $k_{OH,BENZ}$=1.22x10^{-12}, $k_{OH,TOL}$=5.63x10^{-12}, $k_{OH,XYL/EBENZ}$=(7-23)x10^{-12}, $k_{OH,C3\text{-}BENZ}$=(6-57)x10^{-12}, $k_{OH,CO}$=1.5x10^{-13} (from IUPAC, 2005), $k_{OH,BuOH\text{-}D9}$=3.4x10^{-12} (from Barmet et al., 2012) cm^3 molec s^{-1} s^{-1} and used a concentration average of expt A1 of c_{BENZ}=4x10^{11}, c_{TOL}=1x10^{12}, $c_{XYL/EBENZ}$=8x10^{11}, $c_{C3\text{-}BENZ}$=2x10^{11}, c_{CO}=(3-7)x10^{14}, $c_{BuOH\text{-}D9}$=(3.7-7.4) x10^{11} in molec cm^{-3} as input. This results in an OHR_{ext} of 70-100 s^{-1}. Based on these input parameters, the model

from (Li et al., 2015) and (Peng et al., 2016; Peng et al., 2015) predicted an $[OH]_{exposure}$ (OH concentration integrated over time, see discussion in main text "OH exposure estimation", in molec cm^{-3} s) in the OFR as follows:

UV100%: $[OH]_{exposure}=(10\text{-}13)x10^{11}$

UV70%: $[OH]_{exposure}=(2.4\text{-}3.1)x10^{11}$

UV50%: $[OH]_{exposure}=(0.35\text{-}0.48)x10^{11}$.

The estimated $[OH]_{exposure}$ (in molec cm^{-3} s) and OH concentration (in molec cm^{-3}), [OH], based on the experimental measurements of the decay of BuOH-D9 correspond instead to

UV100%: $[OH]_{exposure}=(3.0\text{-}5.8)x10^{11}$, i.e. $[OH]=(2.7\text{-}5.2)x10^{9}$

UV70%: $[OH]_{exposure}=(1.6\text{-}2.5)x10^{11}$, i.e. $[OH]=(1.4\text{-}2.2)x10^{9}$

UV50%: $[OH]_{exposure}=(0.31\text{-}0.49)x10^{11}$, i.e. $[OH]=(0.28\text{-}0.44)x10^{9}$

The ratio of OH (measured) to O_3 (measured) remained relatively constant at our test points (OH/O_3 at 100%: $(1.4\text{-}2.6)x10^{-5}$, $(1.9\text{-}3.0)x10^{-5}$ at 70%, $(1.7\text{-}2.6)x10^{-5}$ at 50%). The corresponding OH information derived from measurements in the SC was an $[OH]_{exposure}$ of $1.4x10^{11}$ molec cm^{-3} s at the maximum aging time (after around 2 hours), at a constant $[OH]=2x10^{7}$ molec cm^{-3}.

Non-OH loss analysis (Figure S11) predicted losses of aromatic hydrocarbons as SOA precursors between 10 and 25% by UV185 nm and UV254 nm, but no impact of O_3, (neither $O(^1D)$ or $O(^3P)$) for the OFR-from-SC conditions. This only refers to the reactive interaction of OH vs. the excitation by UV, and does not allow conclusions on the formation of SOA. Also chemistry initiated by UV185 or UV254 may lead to the formation of SOA, and likewise photons may also destruct OH-formed SOA; both processes deserve attention in future research. Additionally, it does not allow conclusions about the interaction of O_3 with double bonds made available by first ring-opening reactions, and potential effects are not taken into account. Under our diluted conditions (initial NO < 100 ppb), we regard the experiments in OFR as low NO conditions as defined by Peng and Jimenez (2017). The dominant SOA precursors found in the exhaust are not reactive towards NO_3 radicals that can be formed in the OFR; potential effects on first generation products were not taken into account, however. A full discussion of this issue was presented by Peng and Jimenez (2017), who state that under conditions with several hundreds of ppb of NO, an $NO_{3exposure}$-to-$OH_{exposure}$ of 0.1-1 may be reached, under which first generation oxidation products (such as phenolic compounds) might be impacted.

(b) Time-Resolved OFR (see results in Figure S12). As input to the model we used $OHR_{ext}=1000\ s^{-1}$ (for experiments conducted with 1 dilution step, 2014) and $OHR_{ext}=100\ s^{-1}$ for experiments with 2 dilution steps (2015), $[O_3]=1.97x10^{14}$ molec cm^{-3}, a water mixing ratio=0.005 (0.5% absolute humidity, corresponding to ~20% RH at 25°C) and a residence time=100 s. Based on these parameters, the model predicted an $[OH]_{exposure}=(5.9)x10^{10}$ molec cm^{-3} s. For the 2015

experiments (OHR_{ext}=100 s^{-1}) the conditions discussed in (a) applied (Figure S11). Due to the lower dilution ratio in the time-resolved OFR experiments in 2014, however, a significant fraction of the emissions (up to 50-60% of the ArHC) might be lost with UV185 and UV254 nm radicals instead of OH, as a high OHR_{ext} leads to OH suppression in the reactor, making non-OH processes relatively more important. Also $O(^1D)$ and $O(^3P)$ reduce ArHC by ca 10-20% under these conditions (Figure S12). Potential effects of O_3 on first generation products are not taken into account analogously to (a). As detailed in Peng and Jimenez (2017), the NO_x/VOC ratio is a function of the driving cycle. Under conditions with insufficient dilution during time-resolved measurements conducted in 2014, we cannot exclude the influence of NO and NO_3 during simulated photochemical aging, as NO levels had reached "a few ppm levels" during the initial phases of the test cycles. During time-resolved measurements conducted in 2015 (double dilution), NO levels were on the order of a few hundreds of ppb and based on this we estimate no significant impact on our 2015 time-resolved SOA profiles, or the integrated SOA mass. Again, for a full discussion of this issue please refer to Peng and Jimenez (2017).

Quantitative use of OFR data (OFR-from-SC and time-resolved OFR). The SOA yields analysis in the main text is based on SC and OFR-from-SC experiments only. SOA emission factors (EF) are calculated mainly from OFR-from-SC experiments, and additionally, time-resolved data from 2015 collected with GDI4 were integrated to derived EFs labelled "Online, OFR100%" (Sections 3.1, 3.2 and 3.4, Figures 2b, Figure 4) and were comparable to data derived from GDI4 SC experiments. Time-resolved SOA data from 2014 instead were not used quantitatively herein, due to instabilities with the OH exposure throughout the driving cycle (lower OH exposure during high emissions period as well as potential impacts by photolysis and competing non-OH processes (i.e. high external OH reactivity (OHR_{ext}, see Figure S12), and potential NO_x impacts on the oxidation regime (high vs. low NO levels, as discussed above). While these processes limited the use of time-resolved data collected in 2014 due to the low dilution ratio that was applied (only one-fold dilution, i.e. 1 ejector dilutor, 1:8, and additional 1:2 at OFR entrance) and the resulting high OHR_{ext} (>1000 s^{-1}, see Eq. S2, and NO_x levels), data from 2015 were not significantly impacted (an example is given in Figure S14 for GDI4 in standard configuration and w/catGPF), as such experimental artefacts were reduced by use of a higher dilution ratio (2 ejector dilutors in series, 2x 1:8 and additional 1:2 at OFR entrance, OHR_{ext} on the order of 100 s^{-1}). We would like to add that while we don't rely on an absolute quantitative use of our time-resolved data from 2014, the relative time-resolved profile was confirmed in the 2015 data set (Figure S14). Future work should investigate the quantitative use of online OFR data in further detail for additional quantification of cold- and hot-start contribution of SOA to the total SOA burden; a discussion of the associated technical issues (i.e. changes in OH-exposure and condensational sink as well as the equilibration time inside the OFR reactor) has been recently published by Zhao et al. (2018).

S5. O_2^+ charging and fragmentation in the PTR-ToF-MS

While the primary ionization pathway in the PTR-ToF-MS is proton transfer reaction by H_3O^+ ions, the ion source produced up to 5% of unwanted O_2^+. O_2^+ can lead to charge transfer or hydride abstraction reactions (Amador Muñoz et al., 2016; Jordan et al., 2011; Knighton et al., 2009). Signals at $[C_6H_6]^+$ (*m/z* 78), $[C_7H_8]^+$ (*m/z* 92) and $[C_8H_{10}]^+$ (*m/z* 106) likely derive from O_2^+ charged ions of aromatic hydrocarbons (ArHC), and were hence excluded from the analysis of the total mass. However, they supported peak identification by correlation with their corresponding protonated ion at ~5% of the protonated signal. Other ions derived from O_2^+ ionization were insignificant contributors to the total mass.

Frequently, $[C_3H_5]^+$ and $[C_3H_7]^+$ are considered fragments of oxygenated parent molecules. In our experiments, however, these ions may dominantly derive from propene (C_3H_6), for which protonation led to $[C_3H_6{+}H]^+$, and a subsequent loss of H_2 led to $[C_3H_5]^+$. The observed ratio of $[C_3H_5]^+$ and $[C_3H_7]^+$ was consistent with the ratio seen for pure propene (C_3H_6) injected into the instrument as reference (Figure S15). In analogy to O_2^+ ionization of ArHC, we found $[C_3H_6]^+$ in the spectra as insignificant signal (5% of $[C_3H_6{+}H]^+$). It is likely related to an O_2^+ charge transfer to propene (Amador Muñoz et al., 2016; Jordan et al., 2011; Knighton et al., 2009), and supported the peak identification. The fuel contained 5%$_{vol}$ (2014) to 8%$_{vol}$ (2015) of methyl-tert-butyl-ether (MTBE), as an anti-knocking agent. Fragmentation by proton transfer reactions of MTBE can lead to a significant signal at *m/z* 57 ($[C_4H_9]^+$). Protonated butene would also yield $[C_4H_9]^+$, but analogous to the ArHC and propene, should also give a correlated signal at $[C_4H_8]^+$ at approximately 5% of $[C_4H_9]^+$, which we did not observe.

The fragmentation process of alkyl-substituted mono-aromatics would result into a significant mass loss, as the aromatic ring would remain predominantly neutral (especially for mono-aromatics with long alkyl-substituents following Gueneron et al., 2015). For example, only 22% of the ion signal generated from n-pentylbenzene fragmentation retains the aromatic ring (19% $M{+}H^+$, 3% protonated benzene ring), and 88% is found at non-aromatic ions *m/z* 41 or 43). Alkyl-substituted monocylic aromatics might hence (together with long-chain aliphatic compounds which might also substantially fragment) be significant contributors to the missing carbon mass (on average 35%), based on a comparison of FID-based and PTR-ToF-MS based measurements.

SI Figures

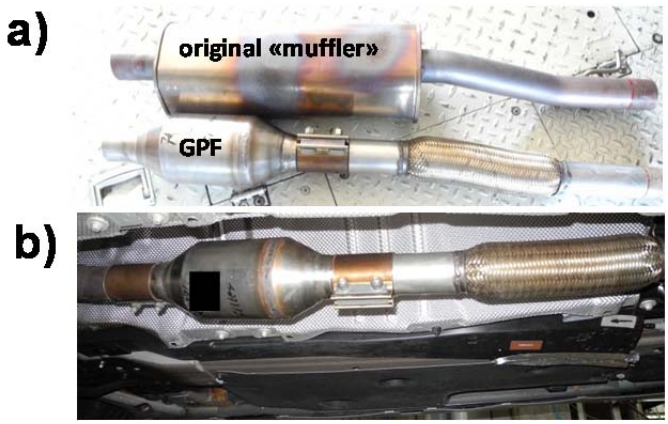

Figure S1. Pictures of **a)** original "muffler" and GPF in comparison**, b)** retrofitted GPF, installed underfloor in replacement to "muffler".

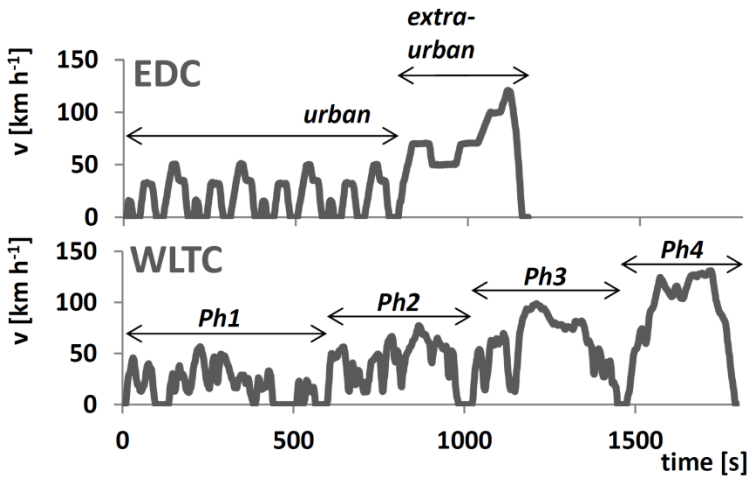

Figure S2. Speed profile of regulatory driving tests. Speed profile (v, in km h^{-1}) versus test time (in seconds) of EDC (new European driving cycle, top) and WLTC (world-wide light duty test cycle, class-3, bottom). While the EDC is characterized by two phase (an urban, and an extra-urban phase of highly repetitive characteristics) and lasts 20 min, the WLTC (class-3) is characterized by four phases at different speed levels (referred to as Phase (Ph) 1-4, or low, medium, high, and extra-high speed, respectively); it contains patterns of disruptive acceleration and deceleration, and lasts 30 min. The WLTC is believed to represent typical driving conditions around the world and was developed based on combination of collected in-use data and suitable weighting factors by an expert group from China, EU, India, Japan, South Korea, Switzerland and the USA.

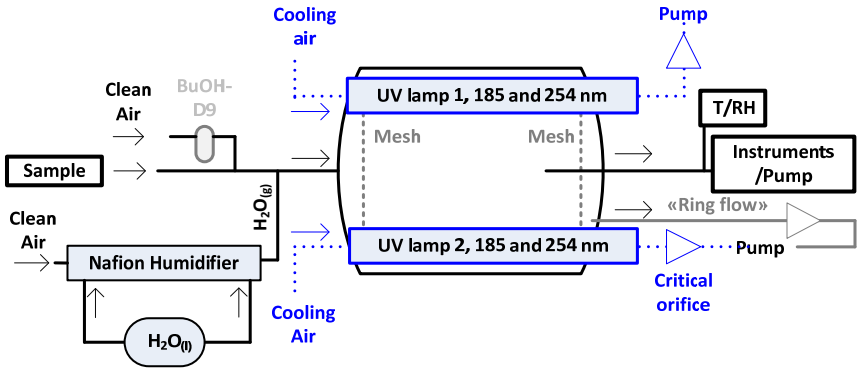

Figure S3. OFR schematic (not to scale). The OFR version deployed here was previously described in Bruns et al. (2015). The reactor is a 0.015 m^3, cylindrical glass chamber (0.46 m L, 0.22 m diameter) flanked by two UV lamps on the upper part of the reactor, each with discrete emission lines at 185 and 254 nm (BHK Inc.). The lamps are cooled by a constant flow of air, or N_2. The incoming reactant flow is radially dispersed in the OFR by passing through a perforated mesh screen at the inlet flange. The flow through the OFR is determined by the flow pulled by instruments and pumps behind the reactor. The reactor is equipped with an injection system for water vapor (H_2O) and NMOCs (notably BuOH-D9, and selected precursor for single molecule testing). Water vapor is provided via a Nafion humidifier. Air is passing on one side of the Nafion membrane, collecting water vapor from the liquid on the other side of the membrane. In addition, other chemicals, such as BuOH-D9 (used as an OH tracer) can be injected by passing a small stream of clean air through a vial containing the liquid NMOC.

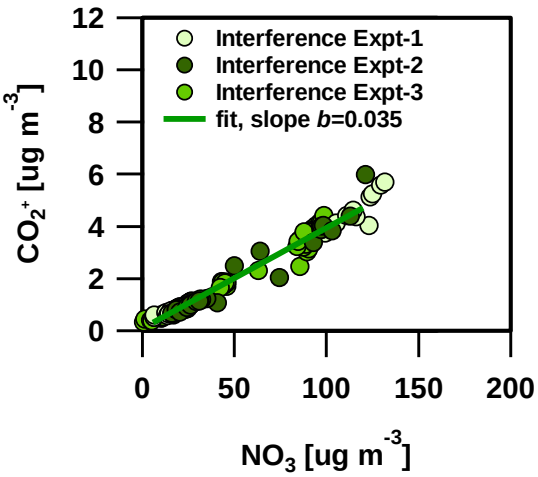

Figure S4. Ammonium nitrate (NH_4NO_3) interference on CO_2^+ (Pieber et al., 2016). The CO_2^+ signal (RIE=1) vs the NO_3 signal (RIE=1) from pure ammonium nitrate (NH_4NO_3) aerosol with d_m=400 nm from 3 calibration experiments. An orthogonal distance least squares fit yields a slope of b=0.035. Corrections were applied via the fragmentation table as noted in the main text.

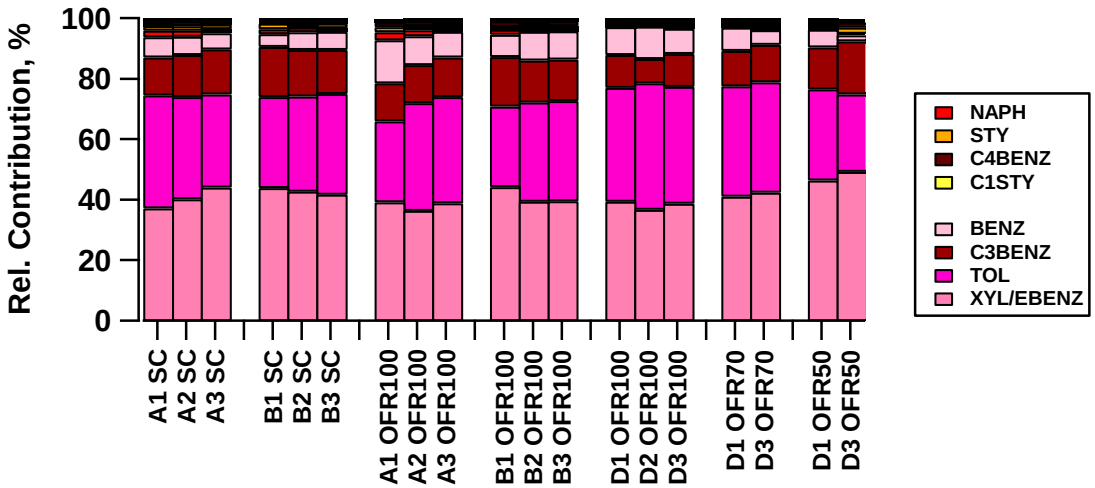

Figure S5. Reacted NMOC fraction in the SC (2h after UV on), and the OFR at 100, 70 and 50% UV intensity (8 dominant ArHC). A-D identifiers refer to individual experiments (GDI 1 only). The final OH exposure in the SC compares to an OH exposure of the OFR at 50-70% UV setting.

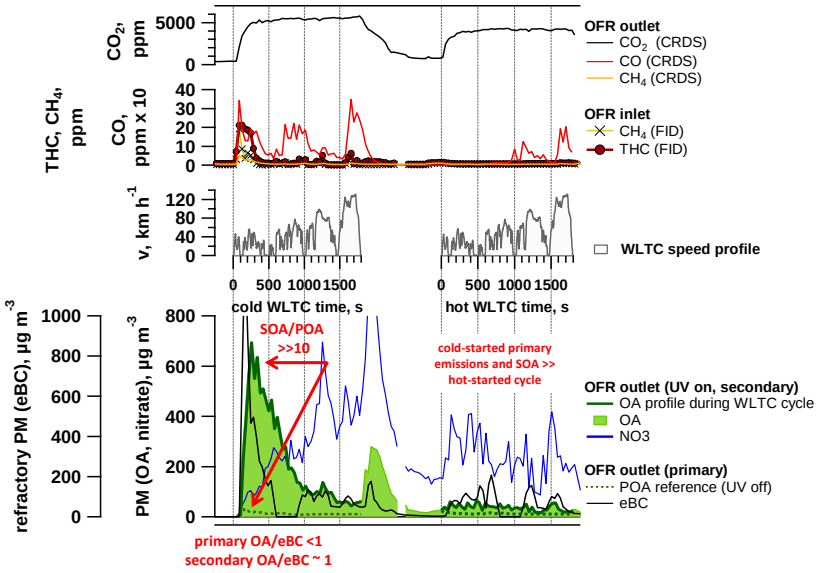

Figure S6. Time-resolved aging of emissions (WLTC) (GDI1, standard configuration, Expt A1). Cold and hot started WLTC of vehicle GDI1 (standard configuration). CO_2. CO, CH_4 (as measured by CRDS), THC and CH_4 (as measured by FID, note that the THC signal reaches its range limit at 20 ppm) are presented, together with organic aerosol (primary (denoted POA) and total (POA+SOA), denoted as OA. "OA profile during WLTC" highlights the measurement during the driving cycle, whereas OA shows the extended signal taking into account a delay due to the OFR residence time. Secondary nitrate aerosol (inorganic, ammonium nitrate, displayed is only NO_3), and primary equivalent black carbon (eBC). Note: data in these graphs are not normalized to CO_2, and have slightly different dilution ratios between cold- and hot-started cycle, as indicated by the CO_2 time-trace. Data reflect measured concentrations; no dilution corrections are applied. CRDS was diluted by a factor of 10 compared to FID and particle phase measurements.

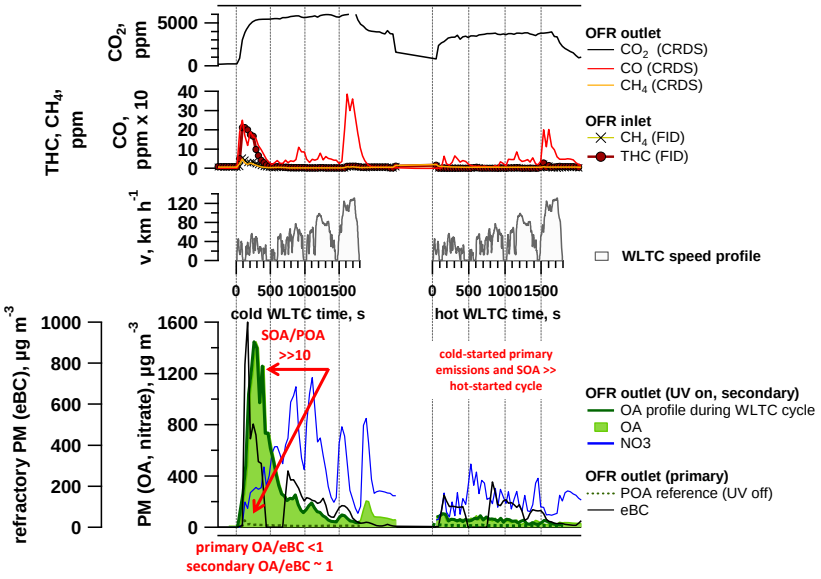

Figure S7. Time-resolved aging of emissions (WLTC) (GDI1, standard configuration, Expt A2, extended version of main text Figure 3). See Figure S6 caption for further details.

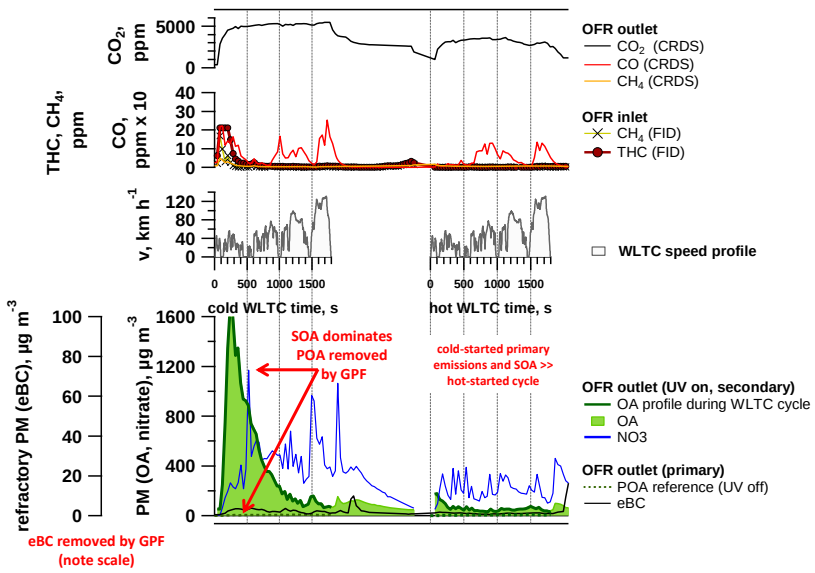

Figure S8. Time-resolved aging of emissions (WLTC) (GDI1 w/ GPF, Expt B1). See Figure S6 caption for further details.

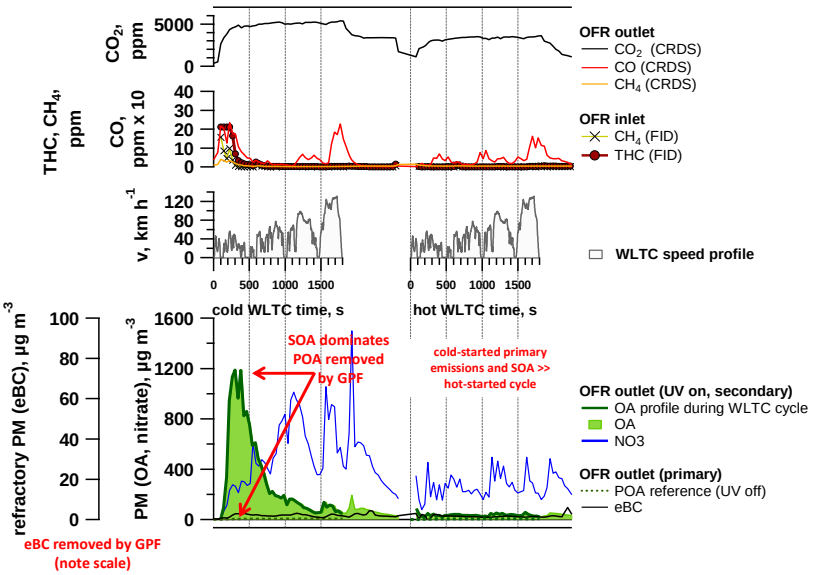

Figure S9. Time-resolved aging of emissions (WLTC) (GDI1 w/ GPF, Expt B2). See Figure S6 caption for further details.

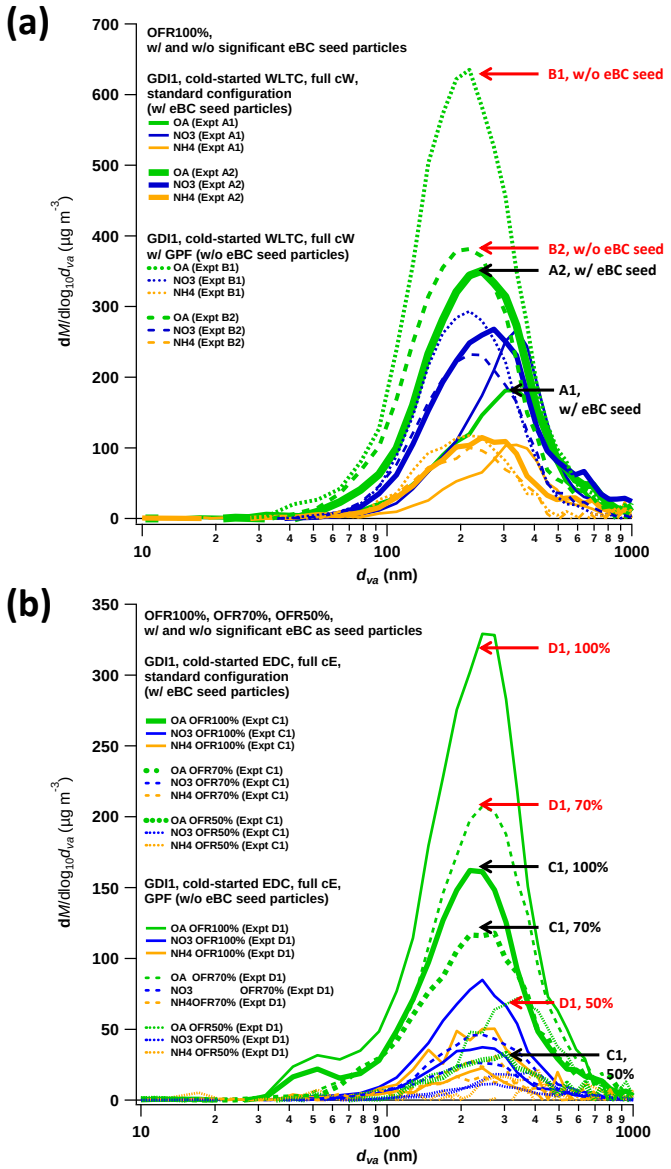

Figure S10. Particle size distributions for experiments from (a) WLTC and (b) EDC, measured behind the OFR-from-SC. All OFR-from-SC tests leading to typically 200 µg m^{-3} (~100-500 µg m^{-3}) SOA formed at 100%, down to ~50 µg m^{-3} for 50% UV conditions. Expt A-D are identifiers for experiments referring to Table S4.

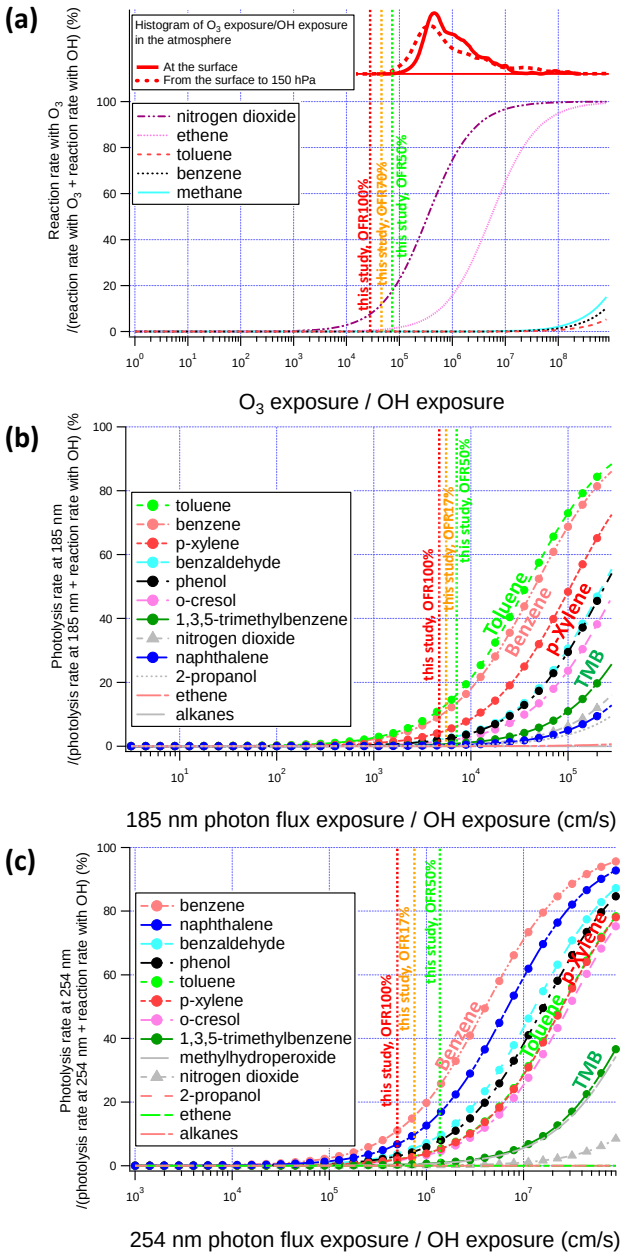

Figure S11. OFR-from-SC and Online OFR 2015: non-OH loss estimation (OFR model by Peng et al. (2016); settings: "OFR185 Option 2"). Results are presented for OFR-from-SC Expts at 100% UV intensity, i.e. [OH]= 2.7-5.2 10^9 molec cm^{-3}. (a) O_3, (b) 185 nm, (c) 254 nm. Input parameters to "2016-10-12_OFR_Exposures_Estimator_v2.3": OHR_{ext}=100 s^{-1}, [O_3]=1.97 x 10^{14} molec cm^{-3} (at 100%), [O_3]=0.74 x 10^{14} molec cm^{-3} (at 70%), [O_3]=0.17 x 10^{14} molec cm^{-3} (at 50%), water mixing ratio = 0.01 (1% absolute humidity).

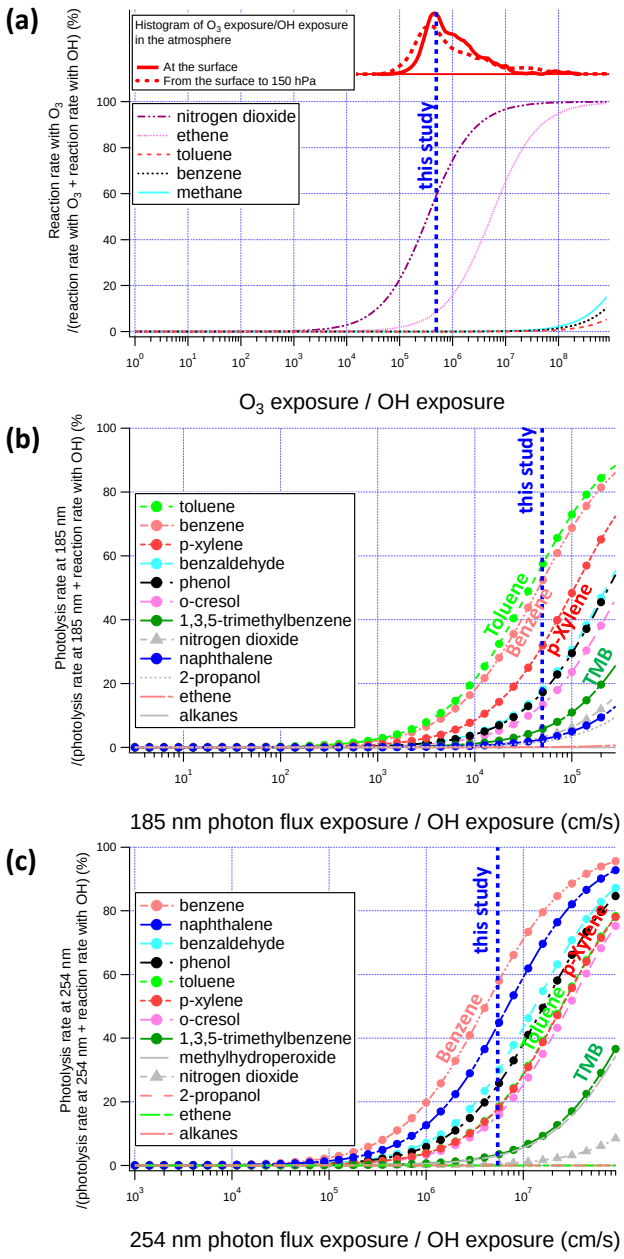

Figure S12. Online OFR 2014: Non-OH loss estimation (OFR model by Peng et al. (2016); settings: "OFR185 Option 2"). Time-resolved OFR Expts at 100% UV intensity (GDI1, 1 ejector dilution). (a) O_3, (b) 185 nm, (c) 254 nm. Input parameters to "2016-10-12_OFR_Exposures_Estimator_v2.3": OHR_{ext}=1000 s^{-1}, $[O_3]$=1.97x10^{14} molec cm^{-3}, water mixing ratio=0.005 (0.5% absolute humidity), residence time=100 s; model-predicted OH-exposure=(5.9)x10^{10} molec cm^{-3} s.

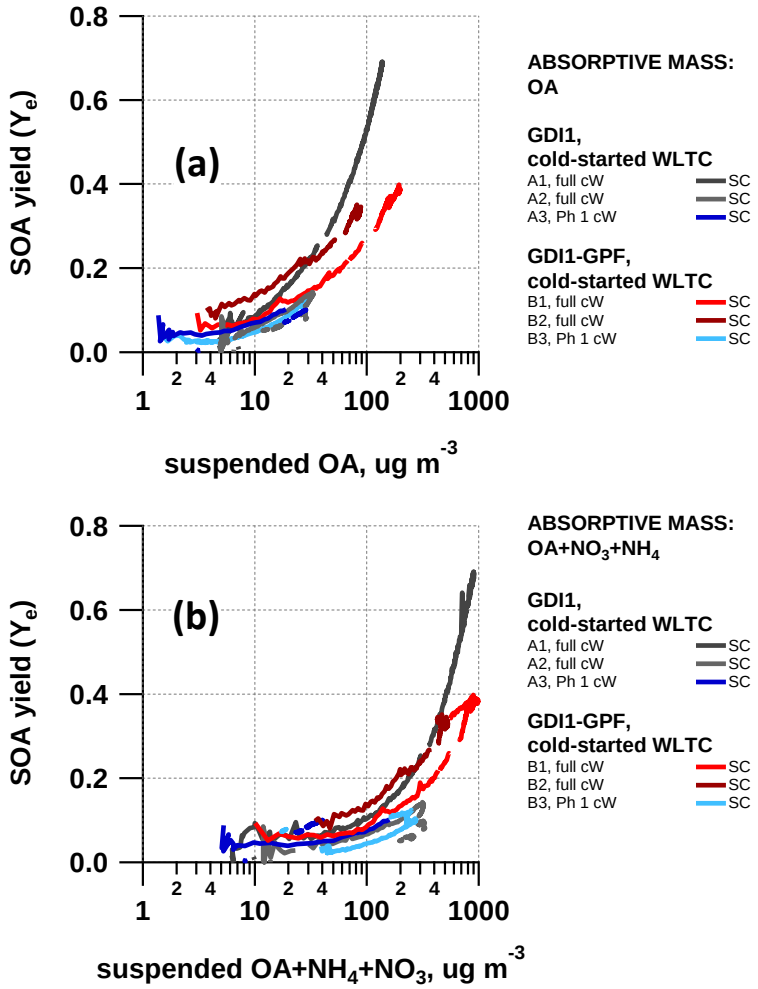

Figure S13. Effective SOA yields from SC experiments with different assumptions of absorptive mass. (a) Yields as a function of suspended OA concentration, and **(b)** as a function of the sum of OA, HR-ToF-AMS derived ammonia (NH_4) and nitrate (NO_3), assuming that NH_4NO_3 acts as additional absorptive mass. Identifiers (A1-A3, B1-B3) allow retrieving the SC experimental conditions for each experiment from Table S4-S7.

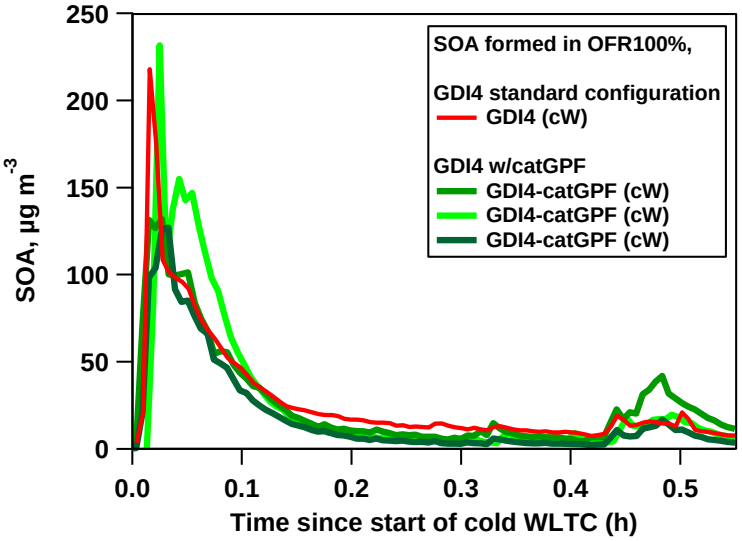

Figure S14. Time-resolved SOA from GDI4 in standard configuration and equipped with a prototype, catalytically active GPF. SOA was generated by exposure of emissions to photochemistry in the OFR during cold-started WLTC test bench experiments.

5

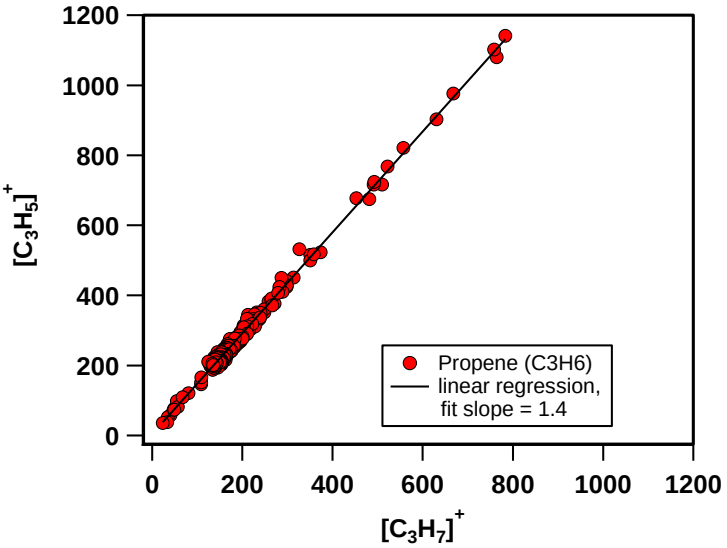

Figure S15. Propene fragmentation ratio in the PTR-ToF-MS. Measurements were conducted at a concentration of around 0-150 ppbv propene (C_3H_6), as measured by the FID instrument.

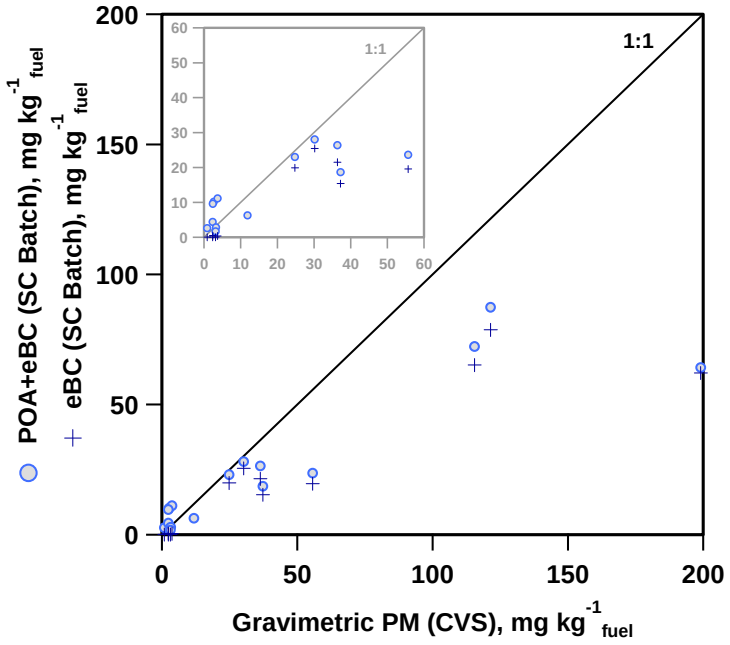

Figure S16. POA and eBC measurements in the SC batch sample compared to gravimetric PM measurements from the CVS (a zoomed-in version is embedded in the figure).

3 SI Tables

Table S1. Vehicle specifications.

Parameters	GDI1	GDI2	GDI3	GDI4
Vehicle Type	Opel Insignia 1.6 EcoFlex	Opel Zafira Tourer	VW Golf Plus	Volvo V60 T4F
Engine code	A16XHT	A16XHT	CAV	B4164T2
Cylinder (number/ arrangement)	4 / in line	4 / in line	4 / in line	4 / in line
Displacement,cm3	1598	1598	1390	1596
Power, kW	125 @ 6000 rpm	125 @ 6000 rpm	118 @ 5800 rpm	132 @ 5700 rpm
Torque, Nm	260 @ 1650-3200 rpm	260 @ 1650 - 3200 rpm	240 @ 1500 rpm	240 @ 1600 rpm
Injection type	DI	DI	DI	DI
Curb weight, kg	1701	1678	1348 - 1362	1554
Gross vehicle weight, kg	2120	2360	1960 - 1980	2110
Drive wheel	Front-wheel drive	Front-wheel drive	Front-wheel drive	Front-wheel drive
Gearbox	m6	m6	m6	a6
First registration	2014	22.07.2014	01.02.2010	27.01.2012
Exhaust	EURO 5b+	EURO 5b+	EURO 4	EURO 5a
VIN	YV1FW075BC1043598	WOLPD9EZ0E2096446	WVWZZZ1KZ9W844855	YV1FW075BC1043598

Table S2. Gas-phase instrumentation.

Gas phase Instruments	Measured Parameter	Manufacturer	Lower limit (or range)
Picarro Cavity Ring-Down Spectrometer G2401	$CO_2 + CO + CH_4 + H_2O$	Picarro	0-1000 ppmC (CO_2) 0-5 ppmC (CO) 0-20 ppmC (CH_4) 0-7% (H_2O)
THC Monitor APHA-370	Total Hydrocarbon (THC), Non-methane hydrocarbon (NMHC)	Horiba	0.02-100 ppmC
Proton-Transfer-Reaction-Time-of-Flight-Mass Spectrometer (PTR-ToF-8000)	Volatile organic compounds (VOC)	Ionicon Analytik	10 ppt

Table S3. Particle-phase instrumentation.

Particle Phase Instruments	Measured Parameter	Manufacturer	Lower limit or (range)
High Resolution-Aerosol-Time-of-Flight-Mass Spectrometer (HR-ToF-AMS)	Size resolved non-refractory particulate matter	Aerodyne	1μg m^{-3}, d_P 0.1-1 μm
Scanning Mobility Particle Sizer (SMPS)	Number-weighted aerosol size distribution	Home built, with TSI DMA, and 3022 CPC	0.01 particles cm^{-3}, d_P 15-850 nm
Aethalometer AE33	Equivalent Black Carbon (eBC)	Aerosol d.o.o	10 ng m^{-3}-100 ng m^{-3}
Condensation particle counter CPC 3776	Particle number	TSI	0.01-10^7 particles cm^{-3}, d_P ≥4nm

Table S4. Average concentration after sampling into the SC, formed in the SC or OFR-from-SC (GDI1, cold-started WTLC and EDC).

Expt	Veh.	Test cycle[#]	Ph	NMHC (FID)	CO	CO_2	NO_x	NMHC/ NO_x	NMOC (PTR)	NMOC (PTR)	ArHC (PTR)	eBC	POA	SOA*	Nitrate*
				ppbC	ppm	ppm	ppb	ppbC ppb^{-1}	µg m^{-3}	µgC m^{-3}	µg m^{-3}	µg m^{-3}	µg m^{-3}	µg m^{-3}	µg m^{-3}
A1	GDI1	cW	full cW	1610	47	1717	72	22	586	462	358	58	6.4	134 (128")	606 (134")
A2	GDI1	cW	full cW	1700	36	1909	62	27	575	180	428	53	5.7	32 (266")	217 (185")
A3	GDI1	cW	Ph 1	2280	17	700	25	91	762	670	669	33	2.8	61 (275")	29.9 (99")
A4	GDI1	cW	Ph 2-4	274	24	1328	33	8	146	93	26	9.7	1.9	2.8 (5.4")	198 (50")
B1	GDI1-GPF	cW	full cW	2400	41	2123	58	41	891	776	759	0.05	2.4	195 (486")	625 (185")
B2	GDI1-GPF	cW	full cW	1800	29	1766	56	32	558	481	458	0.05	3.3	87 (305")	347 (156")
B3	GDI1-GPF	cW	Ph 1	1540	15	592	23	66	433	370	361	0.2	1.4	28 (206")	189 (99")
B4	GDI1-GPF	cW	Ph 2-4	182	21	1240	47	4	16	12	4	0.2	1.6	2.5 (12")	64 (144")
C1	GDI1	cE	full cE	1870	12	1304	41	46	440	390	391	21	3.7	120"	19"
D1	GDI1-GPF	cE	full cE	1830	12	1235	32	58	479	413	397	0.05	1.4	239"	43"
D2	GDI1-GPF	cE	full cE	1770	12	1250	34	52	457	396	388	n.a.	1.5	255"	86"
D3	GDI1-GPF	cE	full cE	2020	14	1650	38	53	497	439	447	0.05	1.2	255"	57"

[#]cW refers to cold-started WLTC, cE refers to cold-started EDC cycle; the driving tests were conducted over the full cycle, Ph 1, Ph 2-4 and "full" indications refer to selective sampling of driving cycle phases into the SC and hence presents average exhaust gas concentrations as input to SC (A1-B4) and OFR-from-SC (A1-D3) photochemical experiments. Online time-resolved tests were monitored and emissions were photochemically aged in the OFR over the full driving cycle for each driving test (integrated data are, however, not presented herein except for GDI4 in 2015). *secondary aerosol mass formed upon simulated photochemistry (SC experiments, "OFR-from-SC experiments UV100), not wlc). n.a.=data not available.

Table S5. Average concentration after sampling into the SC, formed in OFR-from-SC (GDI2, cold-started WLTC).

Expt	Veh.	Test cycle[#]	Ph	NMHC (FID)	CO	CO_2	NO_x	NMHC/ NO_x	NMOC (PTR)	NMOC (PTR)	ArHC (PTR)	eBC	POA	SOA*	Nitrate*
				ppbC	ppm	ppm	ppb	ppbC ppb^{-1}	µg m^{-3}	µgC m^{-3}	µg m^{-3}	µg m^{-3}	µg m^{-3}	µg m^{-3}	µg m^{-3}
E1	GDI2	cW	full cW	996	8.05	1334	n.a.	n.a.	634	460	315	n.a.	3.5	70“	10“
E2	GDI2	cW	full cW	1430	12.7	1303	n.a.	n.a.	771	575	412	25.1	3.9	129“	24.6“
E3	GDI2	cW	full cW	n.a.	8.4	1003	n.a.	n.a.	504	400	265	9.07	2.1	94“	33.1“
E4	GDI2	cW	Ph 1	n.a.	7.6	398	n.a.	n.a.	378	332	326	7.64	1.1	118“	29.5“

[#]cW refers to cold-started WLTC, cE refers to cold-started EDC cycle; the driving tests were conducted over the full cycle, Ph 1, Ph 2-4 and “full” indications refer to selective sampling of driving cycle phases into the SC and hence presents average exhaust gas concentrations as input to OFR-from-SC photochemical experiments. Online time-resolved tests were monitored and emissions were photochemically aged in the OFR over the full driving cycle for each driving test (integrated data are, however, not presented herein except for GDI4 in 2015). *secondary aerosol mass formed upon simulated photochemistry (“OFR-from-SC experiments UV100). n.a.=data not available.

Table S6. Average concentration after sampling into the SC, formed OFR-from-SC (GDI3, cold-started WLTC).

Expt	Veh.	Test cycle[#]	Ph	NMHC (FID)	CO	CO_2	NO_x	NMHC/ NO_x	NMOC (PTR)	NMOC (PTR)	ArHC (PTR)	eBC	POA	SOA*	Nitrate*
				ppbC	ppm	ppm	ppb	ppbC ppb^{-1}	µg m^{-3}	µgC m^{-3}	µg m^{-3}	µg m^{-3}	µg m^{-3}	µg m^{-3}	µg m^{-3}
F1	GDI3	cW	full cW	1198	10.0	525	n.a.	n.a.	447	380	264	13.9	0.48	123“	267“
F2	GDI3	cW	full cW	n.a.	2.07	485	n.a.	n.a.	229	147	137	8.03	0.96	31.2“	42.4“
F3	GDI3	cW	Ph 1	n.a.	1.47	158	n.a.	n.a.	202	154	121	5.45	1.06	26.4“	52.2“
F4	GDI3	cW	Ph 2-4	n.a.	0.49	339	n.a.	n.a.	191	101	33	2.16	0.05	2.3“	65.1“

[#]cW refers to cold-started WLTC, cE refers to cold-started EDC cycle; the driving tests were conducted over the full cycle, Ph 1, Ph 2-4 and “full” indications refer to selective sampling of driving cycle phases into the SC and hence presents average exhaust gas concentrations as input to OFR-from-SC photochemical experiments. Online time-resolved tests were monitored and emissions were photochemically aged in the OFR over the full driving cycle for each driving test (integrated data are, however, not presented herein except for GDI4 in 2015). *secondary aerosol mass formed upon simulated photochemistry (“OFR-from-SC experiments UV100). n.a.=data not available.

Table S7. Average concentration after sampling into the SC, formed in SC (GDI4, cold-started WLTC).

Expt	Veh.	Test cycle[#]	Ph	NMHC (FID)	CO	CO_2	NO_x	NMHC/ NO_x	NMOC (PTR)	NMOC (PTR)	ArHC (PTR)	eBC	POA	SOA*	Nitrate*
				ppbC	ppm	ppm	ppb	ppbC ppb^{-1}	µg m^{-3}	µgC m^{-3}	µg m^{-3}	µg m^{-3}	µg m^{-3}	µg m^{-3}	µg m^{-3}
G1	GDI4	cW	full cW	438	6.01	1218	n.a.	n.a.	429	180	169	9.99	n.a.	10.1	9.1
G2	GDI4	cW	full cW	486	7.03	1555	57	8.5	415	136	177	10.1	2.11	5.1	8.8
G3	GDI4	cW	full cW	750	10.1	1830	112	6.7	508	288	251	14.9	3.05	4.5	27.5
G4	GDI4	cW	full cW	688	n.a.	n.a.	118	5.8	356	215	185	20.1	n.a.	n.a.	n.a.

[#]cW refers to cold-started WLTC, cE refers to cold-started EDC cycle; the driving tests were conducted over the full cycle. Online time-resolved tests were monitored and emissions were photochemically aged in the OFR over the full driving cycle for each driving test (integrated data are, however, not presented herein except for GDI4 in 2015, which are labelled “online OFR” in the corresponding figures in the main text). *secondary aerosol mass formed upon simulated photochemistry (SC experiments, not wlc). n.a.=data not available.

Table S8. OFR yields from this study as presented in Figure 6 in the main text.

Compound	OA µg m^{-3}	OA_err µg m^{-3}	Ye µg ug^{-1}	Ye_err µg ug^{-1}
TOL				
TOL	26	4	0.15	0.02
TOL	50	8	0.18	0.03
TOL	66	10	0.21	0.03
TOL	69	10	0.19	0.03
TOL	70	11	0.16	0.02
TOL	106	16	0.23	0.03
TOL	117	18	0.21	0.03
TOL	291	44	0.29	0.04
TOL	795	119	0.35	0.05
OXYL/TOL (3:1)				
OXYL/TOL (3:1)	347	52	0.64	0.10
OXYL/TOL (3:1)	507	76	0.46	0.07
OXYL/TOL (3:1)	588	88	0.53	0.08
OXYL/TOL (3:1)	852	128	0.76	0.11
OXYL/TOL (10:1)				
OXYL/TOL (10:1)	26	4	0.14	0.02
OXYL/TOL (10:1)	82	12	0.34	0.05
OXYL/TOL (10:1)	104	16	0.26	0.04
OXYL/TOL (10:1)	176	26	0.27	0.04
OXYL/TOL (10:1)	266	40	0.45	0.07
TMB/TOL (2:1)				
TMB/TOL (2:1)	141	21	0.36	0.05
TMB/TOL (2:1)	192	29	0.29	0.04
TMB/TOL (2:1)	195	29	0.37	0.06
TMB/TOL (20:1)				
TMB/TOL (20:1)	675	101	0.45	0.07

References

Amador Muñoz, O., Misztal, P. K., Weber, R., Worton, D. R., Zhang, H., Drozd, G., and Goldstein, A. H.: Sensitive detection of n-alkanes using a mixed ionization mode proton-transfer-reaction-mass spectrometer, Atmos. Meas. Tech., 9, 5315-5329, 10.5194/amt-9-5315-2016, 2016.

Barmet, P., Dommen, J., DeCarlo, P. F., Tritscher, T., Praplan, A. P., Platt, S. M., Prévôt, A. S. H., Donahue, N. M., and Baltensperger, U.: OH clock determination by proton transfer reaction mass spectrometry at an environmental chamber, Atmos. Meas. Tech., 5, 647-656, 10.5194/amt-5-647-2012, 2012.

Bruns, E. A., El Haddad, I., Keller, A., Klein, F., Kumar, N. K., Pieber, S. M., Corbin, J. C., Slowik, J. G., Brune, W. H., Baltensperger, U., and Prévôt, A. S. H.: Inter-comparison of laboratory smog chamber and flow reactor systems on organic aerosol yield and composition, Atmos. Meas. Tech., 8, 2315-2332, 10.5194/amt-8-2315-2015, 2015.

Gueneron, M., Erickson, M. H., Vanderschelden, G. S., and Jobson, B. T.: PTR-MS fragmentation patterns of gasoline hydrocarbons, Int. J. Mass Spectrom., 379, 97-109, 10.1016/j.ijms.2015.01.001, 2015.

IUPAC Task Group on Atmospheric Chemical Kinetic Data Evaluation – Data Sheet HOx_VOC10 (last updated January 12, 2005). http://iupac.pole-ether.fr/. (accessed February 12, 2017), International Union of Pure and Applied Chemistry, 2005.

Jordan, A., Jaksch, S., Jürschik, S., Edtbauer, A., Agarwal, B., Hanel, G., Hartungen, E., Seehauser, H., Märk, L., Sulzer, P., and Märk, T. D.: H_3O^+, NO^+ and O_2^+ as precursor ions in PTR-MS: isomeric VOC compounds and reactions with different chemical groups, 5th International Conference on Proton Transfer Reaction Mass Spectrometry and its Applications, 2011.

Knighton, W. B., Fortner, E. C., Midey, A. J., Viggiano, A. A., Herndon, S. C., Wood, E. C., and Kolb, C. E.: HCN detection with a proton transfer reaction mass spectrometer, Int. J. Mass Spectrom., 283, 112-121, 10.1016/j.ijms.2009.02.013, 2009.

Li, R., Palm, B. B., Ortega, A. M., Hlywiak, J., Hu, W., Peng, Z., Day, D. A., Knote, C., Brune, W. H., de Gouw, J. A., and Jimenez, J. L.: Modeling the radical chemistry in an oxidation flow reactor: radical formation and recycling, sensitivities, and the OH exposure estimation equation, J. Phys. Chem. A, 119, 4418-4432, 10.1021/jp509534k, 2015.

Peng, Z., Day, D. A., Stark, H., Li, R., Lee-Taylor, J., Palm, B. B., Brune, W. H., and Jimenez, J. L.: HOx radical chemistry in oxidation flow reactors with low-pressure mercury lamps systematically examined by modeling, Atmos. Meas. Tech., 8, 4863-4890, 10.5194/amt-8-4863-2015, 2015.

Peng, Z., Day, D. A., Ortega, A. M., Palm, B. B., Hu, W., Stark, H., Li, R., Tsigaridis, K., Brune, W. H., and Jimenez, J. L.: Non-OH chemistry in oxidation flow reactors for the study of atmospheric chemistry systematically examined by modeling, Atmos. Chem. Phys., 16, 4283-4305, 10.5194/acp-16-4283-2016, 2016.

Peng, Z., and Jimenez, J. L.: Modeling of the chemistry in oxidation flow reactors with high initial NO, Atmospheric Chemistry and Physics Discussions, 1-37, 10.5194/acp-2017-266, 2017.

Pieber, S. M., El Haddad, I., Slowik, J. G., Canagaratna, M. R., Jayne, J. T., Platt, S. M., Bozzetti, C., Daellenbach, K. R., Frohlich, R., Vlachou, A., Klein, F., Dommen, J., Miljevic, B., Jimenez, J. L., Worsnop, D. R., Baltensperger, U., and Prévôt, A. S. H.: Inorganic Salt Interference on CO_2^+ in Aerodyne AMS and ACSM Organic Aerosol Composition Studies, Environ Sci Technol, 50, 10494-10503, 10.1021/acs.est.6b01035, 2016.

Platt, S. M., El Haddad, I., Zardini, A. A., Clairotte, M., Astorga, C., Wolf, R., Slowik, J. G., Temime-Roussel, B., Marchand, N., Ježek, I., Drinovec, L., Močnik, G., Möhler, O., Richter, R., Barmet, P., Bianchi, F., Baltensperger, U., and Prévôt, A. S. H.: Secondary organic aerosol formation from gasoline vehicle emissions in a new mobile environmental reaction chamber, Atmos. Chem. Phys., 13, 9141-9158, 10.5194/acp-13-9141-2013, 2013.

Platt, S. M., El Haddad, I., Pieber, S. M., Zardini, A. A., Suarez-Bertoa, R., Clairotte, M., Daellenbach, K. R., Huang, R. J., Slowik, J. G., Hellebust, S., Temime-Roussel, B., Marchand, N., de Gouw, J., Jimenez, J. L., Hayes, P. L., Robinson, A. L., Baltensperger, U., Astorga, C., and Prévôt, A. S. H.: Gasoline cars produce more carbonaceous particulate matter than modern filter-equipped diesel cars, Sci Rep, 7, 4926, 10.1038/s41598-017-03714-9, 2017.

Schwantes, R. H., Schilling, K. A., McVay, R. C., Lignell, H., Coggon, M. M., Zhang, X., Wennberg, P. O., and Seinfeld, J. H.: Formation of highly oxygenated low-volatility products from cresol oxidation, Atmos. Chem. Phys., 17, 3453-3474, 10.5194/acp-17-3453-2017, 2017.

Stirnweis, L., Marcolli, C., Dommen, J., Barmet, P., Frege, C., Platt, S. M., Bruns, E. A., Krapf, M., Slowik, J. G., Wolf, R., Prévôt, A. S. H., Baltensperger, U., and El-Haddad, I.: Assessing the influence of NO_x concentrations and relative humidity on secondary organic aerosol yields from α-pinene photo-oxidation through smog chamber experiments and modelling calculations, Atmos. Chem. Phys., 17, 5035-5061, 10.5194/acp-17-5035-2017, 2017.

Zhao, Y., Saleh, R., Saliba, G., Presto, A. A., Gordon, T. D., Drozd, G. T., Goldstein, A. H., Donahue, N. M., and Robinson, A. L.: Reducing secondary organic aerosol formation from gasoline vehicle exhaust, Proc Natl Acad Sci U S A, 114, 6984-6989, 10.1073/pnas.1620911114, 2017.

Zhao, Y., Lambe, A. T., Saleh, R., Saliba, G., and Robinson, A. L.: Secondary Organic Aerosol Production from Gasoline Vehicle Exhaust: Effects of Engine Technology, Cold Start, and Emission Certification Standard, Environ Sci Technol, 52, 1253-1261, 10.1021/acs.est.7b05045, 2018.